Volume 23
Number 41
7 November 2021
Pages 23393–24064

PCCP

Physical Chemistry Chemical Physics

rsc.li/pccp

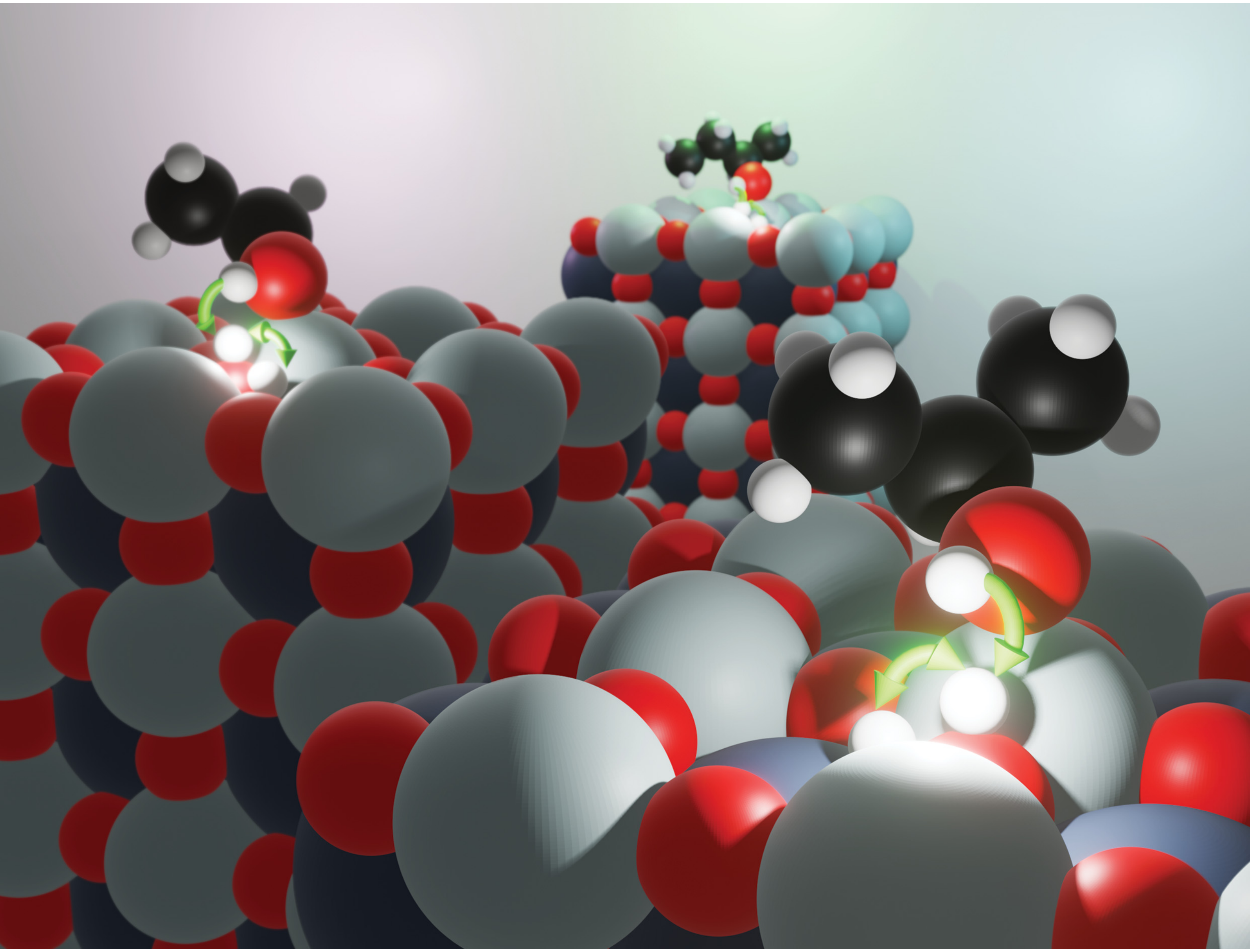

ISSN 1463-9076

ROYAL SOCIETY
OF **CHEMISTRY**

PAPER
Sharani Roy *et al.*
Interfacial acidity on the strontium titanate surface: a scaling paradigm and the role of the hydrogen bond

PCCP

ROYAL SOCIETY OF CHEMISTRY

PAPER

View Article Online
View Journal | View Issue

Cite this: *Phys. Chem. Chem. Phys.*, 2021, **23**, 23478

Received 4th August 2021,
Accepted 16th September 2021

DOI: 10.1039/d1cp03587h

rsc.li/pccp

Interfacial acidity on the strontium titanate surface: a scaling paradigm and the role of the hydrogen bond†‡

Robert C. Chapleski Jr.,[ab] Azhad U. Chowdhury,*[b] Kyle R. Mason,[a] Robert L. Sacci,[b] Benjamin Doughty[b] and Sharani Roy*[a]

A fundamental understanding of acidity at an interface, as mediated by structure and molecule–surface interactions, is essential to elucidate the mechanisms of a range of chemical transformations. While the strength of an acid in homogeneous gas and solution phases is conceptually well understood, acid–base chemistry at heterogeneous interfaces is notoriously more complicated. Using density functional theory and nonlinear vibrational spectroscopy, we present a method to determine the interfacial Brønsted–Lowry acidity of aliphatic alcohols adsorbed on the (100) surface of the model perovskite, strontium titanate. While shorter and less branched alkanols are known to be less acidic in the gas phase and more acidic in solution, here we show that shorter alcohols are less acidic whereas less substituted alkanols are more acidic at the gas–oxide interface. Hydrogen bonding plays a critical role in defining acidity, whereas structure–acidity relationships are dominated by van der Waals interactions between the alcohol and the surface.

1 Introduction

The Brønsted–Lowry strength of an acid in a homogeneous gas or solution is defined by how readily it donates a proton. In a heterogeneous environment, however, where the separation between a donated proton and its conjugate base is determined by the chemical asymmetry of the interface, hydrogen bonding, and molecular ordering, characterizing acidity becomes nebulous. The gas–solid interface complicates the picture of acidity through the adsorption of molecules to specific sites that can tune proton transfer *via* specific molecule–surface interactions. In this scenario, molecular acidity is not determined by the properties of the molecule or the surface independently, but rather by adsorption and interfacial proton dissociation. This complexity motivates us to develop a paradigm of gas–solid interfacial acidity that advances the fundamental description of acid strength beyond that found in homogeneous gaseous or solution environments. Such a paradigm can be then be used to elucidate acid–base reactivity at a range of interfaces.

Perovskites, a broad class of oxide materials, have shown promise in the synthesis of materials ranging from biofuels to pharmaceuticals *via* heterogeneous acid–base catalysis. To date, several studies have pursued a fundamental understanding of the acid–base character of the surface in catalytic reaction mechanisms,[1–9] wherein the acidic or basic nature of metal–oxide surface sites was investigated by monitoring the products of a small alcohol probe molecule, such as isopropanol, reacting at the surface of strontium titanate ($SrTiO_3$, henceforth abbreviated as STO): at an acidic site, a single isopropanol molecule can undergo dehydration to form propylene and water, while at a basic site, acetone and H_2 are formed *via* dehydrogenation.[5,10–16] However, an opposite trend was found for ethanol; Foo *et al.* recently found that the rate of ethanol dehydrogenation increases with the ratio of acidic sites on multifaceted STO nanocubes.[3] This apparent contradiction emphasizes the need to understand the acidity of alkanols at an oxide surface and clarify the mechanisms that control it at the molecular level.

We elucidate the scaling of interfacial acidity of a family of small alkanols with structural and chemical variations when

---

[a] *Department of Chemistry, University of Tennessee, Knoxville, TN 37996, USA. E-mail: sharani.roy@utk.edu*

[b] *Chemical Sciences Division, Oak Ridge National Laboratory, Oak Ridge, TN 37831, USA*

† This manuscript has been authored by UT-Battelle, LLC under Contract No. DE-AC05-00OR22725 with the U.S. Department of Energy. The United States Government retains and the publisher, by accepting the article for publication, acknowledges that the United States Government retains a non-exclusive, paid-up, irrevocable, world-wide license to publish or reproduce the published form of this manuscript, or allow others to do so, for United States Government purposes. The Department of Energy will provide public access to these results of federally sponsored research in accordance with the DOE Public Access Plan (http://energy.gov/downloads/doe-public-access-plan).

‡ Electronic supplementary information (ESI) available: Computations of STO surface stability, adsorption potential-energy-surface scan, alkanol adsorption structural and vibrational frequency data, discussion of van der Waals interactions and interfacial acidity, experimental X-ray diffraction, atomic force microscopy surface characterization data, separate file containing the atomic coordinates of all DFT-optimized structures. See DOI: 10.1039/d1cp03587h

adsorbed to a well-defined and atomically flat STO(100) surface using a combination of density functional theory (DFT) and vibrational sum-frequency generation (SFG) methods. SFG experiments selectively probe interfacial molecular species[17–20] by providing vibrational spectra that are compared with DFT results.[15,21] Using this combined DFT+SFG approach, we describe the mechanisms of adsorption and proton transfer in terms of the interactions of aliphatic alcohols with the oxide surface, with a focus on the structure of the alkanol. To this end, we are able to bridge previous theoretical investigations of alkanol adsorption on STO(100),[5] revealing the essential role of hydrogen bonding on the adsorption equilibria. Finally, we describe the interfacial acidity of the series of aliphatic alcohols from methanol to butanol on STO(100) using partition functions constructed from DFT calculations, and compare the structure–acidity relationships to the known, corresponding relationships in the gas phase and in aqueous solution. While the current study focuses on an oxide surface, the proposed paradigm of interfacial acidity might provide mechanistic insight into bond dissociation, radical formation, and radical dissociation involving proton transfer at other complex interfaces.[22,23]

Our investigation commences with a study of the adsorption of isopropanol on the TiO_2-terminated surface of STO(100). In the first section, we compute the pathway for isopropanol adsorption, leading to a description of a two-state equilibrium on the surface. We then implement SFG not only to experimentally verify the presence of this two-state chemisorption equilibrium for isopropanol, but also to reveal similar equilibria for other alkanols on STO(100), with characteristic spectral shifts related to hydrogen-bonding interactions. We ultimately apply these two-state equilibria to calculate the interfacial Brønsted–Lowry acid strengths of alkanols and determine the structural and chemical factors that control the acidity.

2 Methods

2.1 Computational methods

DFT calculations were performed using the Perdew–Burke–Ernzerhof (PBE) exchange–correlation functional[24,25] and Grimme's D3 method of dispersion correction[26,27] within the Vienna ab initio Simulation Package (VASP).[28–30] For all atoms, projector-augmented-wave potentials (PAW) were used to describe electron-core interactions.[31,32] To allow for electron localization on the STO(100) surface, a Hubbard-U correction of 11.0 eV was applied to the 3d orbitals of Ti atoms, using the approach introduced by Dudarev *et al.*[33] This correction was chosen as it resulted in a calculated band gap of 3.24 eV for bulk STO, similar to that found experimentally (3.25 eV).[34] An energy cutoff of 400 eV was used for the planewave basis set, and partial orbital occupancies were described using Gaussian smearing with a width of 0.05 eV. The bulk lattice constant was calculated to be 4.02 Å, in comparison to an experimental value of 3.91 Å.[35]

The TiO_2-terminated STO(100) surface was modeled by a 3 × 3 × 3 supercell with an additional layer of TiO_2 along the z-direction to allow for TiO_2 termination on both sides. A vacuum layer of 24 Å was added above the top surface layer. The total number of atoms in the supercell was 162, and adsorption of one isopropanol molecule created an adsorbate coverage of 1/9 of a monolayer (ML). The Brillouin zone of the cell was sampled using a 3 × 3 × 1 Monkhorst–Pack k-point grid.[36] Geometry optimizations were performed using the quasi-Newton algorithm,[37] allowing the adsorbate species and the top-most layer of STO (57 atoms) to relax until the force on each atom was less than 0.01 eV Å^{-1}. Transition states were calculated using the climbing-image nudged elastic band method.[38]

2.2 Experimental methods

Sample preparation and characterization followed previous work;[15] characterization results are shown in Section II of the ESI.‡ Similarly, a comprehensive description of the SFG spectrometer used in this experiment can be found elsewhere.[39,40] Briefly, the output of a Spectra Physics Spitfire Pro Ti:Sapphire amplifier (output: 6 W, 1 kHz repetition rate, 45 fs pulses, centered near 800 nm) was split into two paths. The first path was directed into an optical parametric amplifier with difference-frequency mixer to generate broadband mid-infrared (IR) pulses tuned to excite the –OH stretching region. Approximately 2.4 W of the remaining laser output was directed into a pulse shaper to produce time-symmetric narrowband near-infrared (NIR) pulses[39,40] used for up-conversion. The polarizations of both arms were passed through polarizers and subsequently rotated with half waveplates before being collinearly combined with a dichroic optic. The beams were focused onto the STO(100) surface at an angle of 60° relative to the surface normal. An achromatic doublet collected the radiated SFG light before being polarization-resolved, filtered, spectrally resolved and detected with a CCD camera. SFG spectra were background-subtracted and scaled by the nonresonant response obtained from the bare STO(100) sample in the PPP polarization combination. The IR beam path and sample-environment enclosures were continuously purged with dry nitrogen to limit IR attenuation from atmospheric water and to limit adsorption of water to the STO(100) interface during measurements.[41,42]

The measured SFG intensity is proportional to the modulus-square of second-order susceptibility, $\chi^{(2)}_{\text{eff}}$, and the incident driving laser fields, E_{IR} and E_{NIR}:

$$I_{\text{SFG}} \sim |\chi^{(2)}_{\text{eff}} E_{\text{IR}} E_{\text{NIR}}|^2. \tag{1}$$

The effective second-order susceptibility, $\chi^{(2)}_{\text{eff}}$, is the sum of resonant and non-resonant, $\chi^{(2)}_{\text{NR}}$, contributions:

$$\chi^{(2)}_{\text{eff}} = \chi^{(2)}_{\text{NR}} + \sum_q^n \frac{A_q}{\omega_{\text{IR}} - \omega_q + i\Gamma_q} \tag{2}$$

where ω_{IR} is the frequency of incident IR laser light, ω_q is the resonance-transition frequency, A_q is the mode-specific amplitude, and Γ_q is related to the linewidth. Eqn (2) shows that when the incident broadband IR light has spectral components that are resonant with molecular vibrations, there is an enhancement in the radiated signal. This enhancement serves to map the vibrational spectrum in an analogous way to conventional IR or Raman spectroscopies but, owing to the even-order field interaction (see eqn (1)), in a surface specific manner.[43] Measured SFG intensity data was fit to eqn (1) and (2) and used in subsequent analysis.

3 Results and discussion

3.1 Molecular physisorption

DFT results for adsorption of isopropanol in four different molecular orientations at the favorable binding site (Ti-atom top site) on the TiO_2-terminated STO(100) surface are shown in Fig. 1. Based on calculated surface and adsorption energies, we find that the TiO_2-termination is energetically more stable than the SrO-termination and thus consider the former exclusively in this work (see ESI,‡ Section I.A). Here, we find that the alcohol prefers to bind *via* a lone pair on the oxygen to a Ti atom, as determined from a two-dimensional adsorption-energy scan along the surface plane (see ESI,‡ Section I.B.). Out-of-plane rotation of the bound alcohol about its C–O bond results in three orientational minima: (a) "α-H close", in which the α-hydrogen points toward the surface (adsorption energy, E_{ads} = 1.25 eV), (b) "CH_3 away", in which one of the methyl groups points away from the surface (E_{ads} = 1.25 eV), and (c) "α-H away", in which the α-hydrogen points away from the surface (E_{ads} = 1.22 eV). In our notation, positive adsorption energies indicate stable adsorption. When the alkoxy oxygen points away from the surface and does not interact with Ti, as in the "OH away" orientation, adsorption is considerably weakened (E_{ads} = 0.42 eV). Notably, the adsorption of isopropanol in any of the four orientations does not cause significant distortion of the surface structure.

3.2 Dissociative chemisorption

DFT results for dissociative adsorption of isopropanol following transfer of the hydroxyl proton from adsorbed isopropanol to the neighboring surface oxygen for the "α-H close", "CH_3 away", and "α-H away" orientations are shown in Fig. 2. Because the "OH away" orientation is comparatively weakly bound and unlikely to undergo proton transfer due to its orientation, it was not included in the remainder of our study. Our computations reveal that proton transfer results in the formation of two adsorption states: one in which the proton is still hydrogen-bonded to the alkoxy oxygen (Fig. 2a), and another in which the hydrogen bond has broken to fully dissociate the proton from the isopropoxide (Fig. 2b). The adsorption energies of the hydrogen-bonded forms are E_{ads}("α-H close") = 1.40 eV, E_{ads}("CH_3 away") = 1.34 eV, and E_{ads}("α-H away") = 1.38 eV, whereas the adsorption energies of the non-hydrogen-bonded forms are E_{ads}("α-H close") = 1.43 eV, E_{ads}("CH_3 away") = 1.48 eV, and E_{ads}("α-H away") = 1.48 eV. A comparison of adsorption energies in Fig. 1 and 2 shows that dissociative chemisorption of isopropanol is more favorable than non-dissociative, molecular physisorption of isopropanol for all molecular orientations. Similarly, the second chemisorbed form possessing no hydrogen bond is adsorbed more strongly than the hydrogen-bonded form. Section I.C of the ESI‡ shows the bond lengths and angles involving the Ti, surface oxygen, alkoxy oxygen, and transferred proton in the physisorbed and chemisorbed forms of isopropanol. Notably, when the hydrogen bond breaks, the proton moves closer to the TiO_2-surface plane to increase

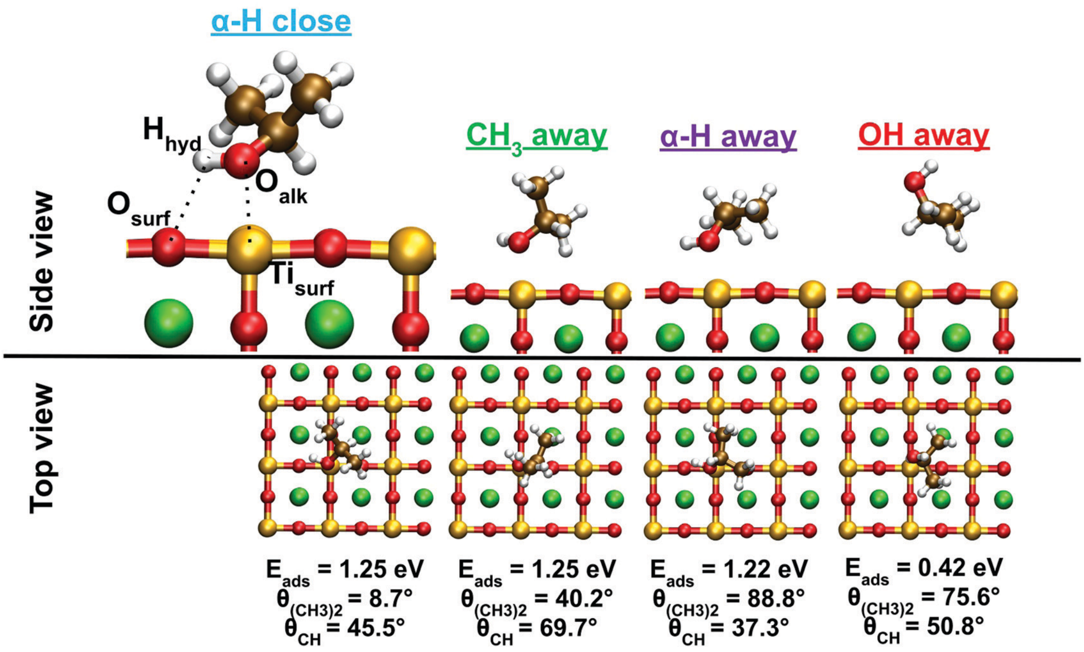

Fig. 1 Side- and top-views of optimized geometries of four different molecular orientations of isopropanol adsorbed on STO(100), calculated using DFT. Below each structure, adsorption energies and orientation angles, $\theta_{(CH_3)_2}$ and θ_{CH} are provided, as described in the text. For "α-H close", dashed lines illustrate bonds that will be formed in subsequent adsorption steps. Color scheme: Sr: green, Ti: yellow, O: red, C: brown, H: white.

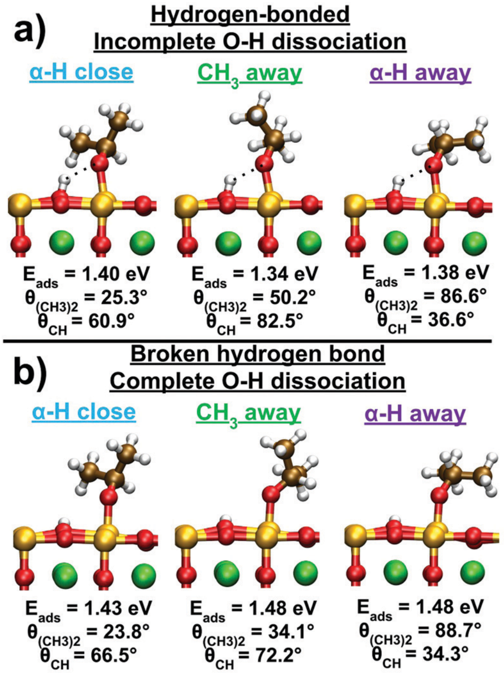

Fig. 2 Side views of optimized geometries of three different orientations of isopropanol on STO(100) following proton transfer, calculated using DFT. Below each structure, its adsorption energy and orientation angles are noted. Structures in (a) exhibit a hydrogen bond (dashed line) between the alkoxy oxygen and the transferred proton, and structures in (b) result from the disruption of this hydrogen bond. Same color scheme as in Fig. 1.

interactions with other nearby surface oxygens. As a result, the angle between the proton–oxygen$_{\text{surface}}$ bond and the surface normal changes from 14–17° in Fig. 2a to 64–66° in Fig. 2b. This large change in the orientation of the bond might have important effects on the subsequent reaction pathways of isopropanol.

3.3 Activation energies of proton transfer

Table 1 shows the calculated activation energies for dissociative chemisorption and subsequent hydrogen-bond breakage of isopropanol on STO(100). The calculated value of 0.24 eV for proton transfer in the "α-H away" orientation is similar to that found in the literature.[5] Zero-point corrections reduce the activation energy for proton transfer to 0.12 ± 0.05 eV and negligibly change the activation energy for hydrogen-bond dissociation. The low values of activation energies suggest that adsorbed isopropanol exists in a thermal equilibrium between the molecular and dissociated forms. A Boltzmann population analysis shows that at 298 K, 0.01% of the adsorbed isopropanol exists in the molecular form, 3.00% exists in the deprotonated and hydrogen-bonded form and 96.98% exists in the deprotonated and hydrogen-bond-broken form. Predictably, an increase in temperature increases the relative population of the hydrogen-bonded form. At 500 K, relevant to the catalytic transformations of isopropanol,[5,15,16] 0.46% of the adsorbed isopropanol exists in the molecular form, 10.98% exists in the deprotonated and hydrogen-bonded form and 88.57% exists in the deprotonated and non-hydrogen-bonded form. Fig. S6 in the ESI‡ shows the energy pathways and Boltzmann populations of all orientations for each adsorbate species at 298 K.

Table 1 DFT-computed activation energies of proton transfer (chemisorption) and subsequent hydrogen-bond dissociation of three orientations of isopropanol adsorbed on STO(100)

Orientation	$\Delta E^{\ddagger}_{\text{proton transfer}}$ (eV)	$\Delta E^{\ddagger}_{\text{H-bond dissociation}}$ (eV)
"α-H close"	0.20	0.03
"CH_3 away"	0.28	0.05
"α-H away"	0.24	0.00

To test the robustness of the computed qualitative differences between the energy pathways of the three orientations, we performed single-point calculations on PBE-optimized geometries and transition states using the RPBE functional,[44] as described in Section I.D. of the ESI.‡ Tables S4–S6 in the ESI‡ show that while the absolute energy of each species is lowered upon change from PBE to RPBE, the energy differences between species are similar between PBE and RPBE. Further, Fig. S7 and S8 in the ESI‡ show energy scans for rotations of the hydrogen-bonded and hydrogen-bond-broken forms of the chemisorbed isopropoxide among their three orientations. The scans show two noteworthy qualitative results. First, the rotational energy barriers are much lower for the hydrogen-bonded than the hydrogen-bond-broken form, suggesting that it is kinetically far more likely for the hydrogen-bonded form to rotate between the three orientations compared to the hydrogen-bond-broken form. Second, the energy barrier to rotate out of the "α-H away" orientation is the highest of the three orientations for both the hydrogen-bonded and hydrogen-bond-broken forms, showing that this orientation is not only thermodynamically, but also kinetically the most stable among the three orientations of the chemisorbed species.

3.4 Spectroscopic signatures of adsorption, proton transfer, and hydrogen bonding

Previous work examined the C–H stretching region of isopropanol adsorbed on STO(100) at 298 K and mapped the absolute orientation of adsorbed isopropanol using SFG methods. One of the key orientational angles was defined as the bisector of the CH_3–C–CH_3 moiety in isopropanol to form an angle, $\theta_{(CH3)2}$, of 29 ± 7° with respect to the surface normal, and another, along the αC–H bond, formed an angle, θ_{CH}, of 51 ± 8°.[15] These measured angles strongly agree with the corresponding calculated angles of the deprotonated forms of isopropanol in the "α-H close" orientation (Fig. 2). This result also corroborates our theoretical results using Boltzmann population analysis (*vide supra*) that the adsorption equilibrium largely favors the chemisorbed over the physisorbed form of isopropanol.

To search for the existence of our DFT-predicted chemisorbed forms of alcohols on STO(100), we measured the SFG spectra in the O–H stretching region for methanol, ethanol, isopropanol, and *sec*-butanol in the SSP polarization combination, with data and fits plotted in Fig. 3. The spectrum of each alcohol adsorbed on STO(100) shows a narrow, intense band at around 3640 cm^{-1} and a broad, lower-intensity band at around 3550–3600 cm^{-1}. Based on a normal-mode analysis of

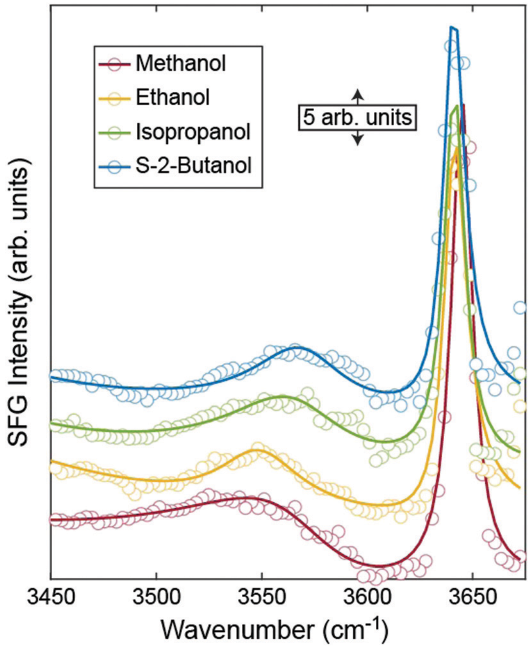

Fig. 3 SFG spectra of methanol, ethanol, isopropanol, and *sec*-butanol (*S*-2-butanol) adsorbed onto STO(100) in the SSP polarization combination. Traces are offset vertically for clarity.

the dissociatively chemisorbed forms of the four alcohols, as shown in Table 2, the broad, lower-frequency band is assigned to the O$_{surface}$-proton stretch when the proton is hydrogen-bonded to the adsorbed alkoxide, and the narrow, higher-frequency band is assigned to the ''free'' O$_{surface}$-proton stretch wherein the hydrogen bond is disrupted. This experimental result with computationally aided assignment directly supports a two-state chemisorption equilibrium. Due to the low Boltzmann population of the physisorbed form of the alcohol, the O$_{alkoxy}$-proton stretch does not appear in the spectrum.

Both DFT and SFG results show very little variation in the O$_{surface}$-proton stretching frequency for the broken-hydrogen-bond species across the four alcohols. In the SFG spectra, these frequencies for ethanol, isopropanol, and *sec*-butanol were nearly identical, and DFT finds a range of only 12 cm^{-1} over corresponding values. This is expected based on the typical ''free'' OH stretching vibrations that do not interact with neighboring species. However, the O$_{surface}$-proton stretching frequencies for the hydrogen-bonded species in the SFG spectra vary over the four alcohols and parallel the frequencies predicted by DFT, with *sec*-butanol > methanol > isopropanol > ethanol. The change in the stretching frequency arises from the increase in the strength of the hydrogen bond, as corroborated by a calculated variation in the lengths of the hydrogen bond (*i.e.*, O$_{alkoxy}$-proton distance): 1.95 Å (*sec*-butanol) > 1.91 Å (methanol) > 1.90 Å (isopropanol) > 1.88 Å (ethanol). This agreement between DFT and SFG reinforces our assignment of the broad band in this region to the O$_{surface}$-proton stretch in the hydrogen-bonded state and suggests that trace amounts of water are not responsible for the measured spectral features. The strength of the hydrogen bond is determined by the competition between the amount of electron density on the alkoxide oxygen and the extent of weakening of alkoxide–surface interactions due to geometric strain from the hydrogen bond. A similar trend is seen for the frequency of the O$_{surface}$-proton wagging mode (see ESI,‡ Table S7), which redshifts with decreasing strengths of the associated hydrogen bond.

Table 2 Unscaled O$_{surface}$-proton stretching frequencies for hydrogen-bonded and broken-hydrogen-bond species of selected alkanols on STO(100), obtained from SFG and DFT. For isopropanol DFT frequencies, the mean frequency and average absolute deviation from the mean computed over three orientations (Fig. 2) are presented. Peak widths are provided for all SFG spectral features

	O$_{surface}$-proton (cm^{-1}) (hydrogen-bonded)		O$_{surface}$-proton (cm^{-1}) (broken hydrogen bond)	
Alcohol	DFT	SFG	DFT	SFG
Methanol	3383	3568/40	3580	3645/6
Ethanol	3331	3548/24	3586	3641/6
Isopropanol	3363 ± 28	3567/34	3581 ± 1	3641/6
sec-Butanol	3440	3570/26	3592	3641/6

Along with frequencies, ranges for O$_{surface}$-proton stretching frequencies derived from DFT results are provided in Table 2. Spectral widths also show agreement between DFT and SFG values. For DFT results, the quoted widths are reported as average absolute deviations from the mean of three frequencies, corresponding to the three orientations shown for each of the two states in Fig. 2 (see ESI,‡ Table S8). Both DFT and SFG affirm that the hydrogen-bonded state results in a broader spectral feature in comparison to the broken-hydrogen-bond state. Notably, a larger sampling of out-of-plane orientations is afforded in the more freely rotating hydrogen-bonded alkoxide compared to the broken-hydrogen-bond state due to a closer O$_{alkoxy}$–Ti distance in the latter form (*vide infra*). This enhanced orientational freedom results in a broader O$_{surface}$-proton stretch in the spectral feature for the hydrogen-bonded species.

3.5 Interfacial acidity

The Brønsted–Lowry acidity ($HA \rightleftharpoons H^+ + A^-$) of an aliphatic alcohol is dictated by the polarizability of the alkyl moiety in the gas phase and solvation of the alcohol in the solution phase. In the gas phase, alkyl substituents on the α-carbon and longer alkyl chains help to polarize the electron cloud on the alkyl moiety in a direction that stabilizes the negative charge on the alkoxide conjugate base. Consequently, the gas-phase acidity increases as: methanol < ethanol < *n*-propanol < *n*-butanol < isopropanol < *tert*-butanol.[45–49] However, in aqueous solution, alkyl substituents on the α-carbon and longer alkyl chains weaken solvation of the conjugate base and increase the entropic penalty to the structure of water. Smaller alcohols and their conjugate bases are more soluble in water, with methoxide showing a greater solvation energy than *tert*-butoxide, for example. Consequently, in small alkanols, the solvation energy overcomes polarization effects, reversing, in solution, the acid-strength trend revealed for the gas phase.[45,46] The question is, how does this dichotomy change at the gas–solid interface?

Based on the two-state chemisorption equilibrium of alkanols on STO(100) described above, we define the interfacial Brønsted–Lowry acidity as: $(\mathrm{H{-}A})_{\mathrm{ads}} \rightleftharpoons \mathrm{H}_{\mathrm{ads}}{}^{+} + \mathrm{A}_{\mathrm{ads}}{}^{-}$, where the hydrogen-bonded species ($(\mathrm{H{-}A})_{\mathrm{ads}}$) serves as the ''acid'' that donates its proton to the surface as the hydrogen bond is broken, resulting in the broken-hydrogen-bond ''conjugate base'' species ($\mathrm{A}_{\mathrm{ads}}{}^{-}$). The interfacial acid (ia) dissociation constant, K_{ia}, is defined as the ratio of temperature-dependent canonical partition functions of the products to the reactant (see ESI,‡ Section I.H.). A stronger acid has a larger K_{ia}, or lower $\mathrm{p}K_{\mathrm{ia}}$ ($= -\log(K_{\mathrm{ia}})$) resulting from the lower free energy associated with the broken-hydrogen-bond species compared to the hydrogen-bonded-species. We note that variations in K_{ia} are dominated by changes in the ratio of electronic partition functions resulting from adsorption energies of the two chemisorbed forms for different alcohols (see ESI,‡ Section I.H).

Fig. 4 shows the $\mathrm{p}K_{\mathrm{ia}}$ of the series of alkanols from methanol to butanol at 298 K, calculated using the most stable orientation for each alkanol. The values of $\mathrm{p}K_{\mathrm{ia}}$ are presented in Table S16 of the ESI.‡ For each alcohol, the most stable orientation of the chemisorbed species is the one that brings the alkyl substituent(s) close to the surface, such as the ''α-H away'' orientations of isopropanol and *sec*-butanol. In the case of linear alcohols, the ''α-H away'' orientation is equivalent to the ''α-H close'' orientation, whereas in the case of *tert*-butanol, all three orientations are equivalent to each other. The optimized structures and adsorption energies for all alkanols are provided in Section I.F of the ESI.‡ The relationships between the structure of the alkanol and its interfacial acidity on STO(100) are revealed by the plots of $\mathrm{p}K_{\mathrm{ia}}$ as a function of the number of carbons atoms, n_{carbons}, (Fig. 4a), and as a function of the number of alkyl substituents on the α carbon, n_{branches}, (Fig. 4b) in the alkanol. The linear fits of $\mathrm{p}K_{\mathrm{ia}}$ values of different groups of alkanols were created to highlight qualitative trends.

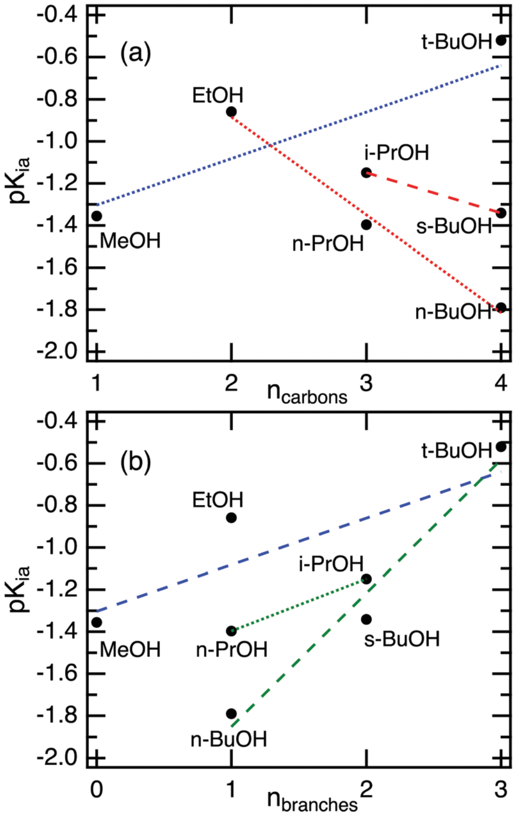

Fig. 4 $\mathrm{p}K_{\mathrm{ia}}$ values for alkanols from methanol to butanol adsorbed on STO(100) at 298 K. DFT-computed values (black circles) are shown as a function of the total number of carbon atoms (n_{carbons}) in (a) and as a function of alkyl substituents on the α-carbon (n_{branches}) in (b). The linear-fit equations in (a) are $\mathrm{p}K_{\mathrm{ia}} = -1.52 + 0.22n_{\mathrm{carbons}}$ (dotted blue, $R^2 = 0.62$), $\mathrm{p}K_{\mathrm{ia}} = 0.05{-}0.46n_{\mathrm{carbons}}$ (dotted red, $R^2 = 0.99$), and $\mathrm{p}K_{\mathrm{ia}} = -0.57$ to $0.19n_{\mathrm{carbons}}$ (dashed red, $R^2 = 1$); and the linear-fit equations in (b) are $\mathrm{p}K_{\mathrm{ia}} = -1.30 + 0.22n_{\mathrm{branches}}$ (dashed blue, $R^2 = 0.62$), $\mathrm{p}K_{\mathrm{ia}} = -1.64 + 0.25n_{\mathrm{branches}}$ (dotted green, $R^2 = 1$), and $\mathrm{p}K_{\mathrm{ia}} = -2.49 + 0.63n_{\mathrm{branches}}$ (dashed green, $R^2 = 0.97$).

While the gas-phase acidity of alcohols increases with n_{carbons} and n_{branches} from methanol to butanol, and the corresponding aqueous acidity decreases with n_{carbons} and n_{branches}, the interfacial acidity increases with n_{carbons} but decreases with n_{branches}. On STO(100), longer alkyl chains stabilize the conjugate base by enhancing van der Waals interactions between the base and the surface, resulting in a decrease in $\mathrm{p}K_{\mathrm{ia}}$ with increase in n_{carbons} as chain lengths are increased at constant α-C substitution (red lines in Fig. 4, see ESI,‡ Section I.H). These interactions increase as the alkoxide approaches closer to the surface in the broken-hydrogen-bond form ($\mathrm{O}_{\mathrm{alkoxy}}$–Ti = 1.91–1.93 Å in the broken-hydrogen-bond form compared to 1.95–1.96 Å in the hydrogen-bonded form across different alcohols). Furthermore, the strain in the $\mathrm{O}_{\mathrm{alkoxy}}$–Ti–$\mathrm{O}_{\mathrm{surface}}$ angle is released, changing from 78–79° in the hydrogen-bonded species to 86–88° as the $\mathrm{O}_{\mathrm{alkoxy}}$–Ti bond is nearly perpendicular to the surface in the broken-hydrogen-bond species. In contrast, greater alkyl substitution on the α-carbon compromises these alkyl-surface interactions in the broken-hydrogen-bond form and linearly increases $\mathrm{p}K_{\mathrm{ia}}$ when the total number of carbons remains constant (green lines in Fig. 4), mainly by decreasing the number of α-hydrogen atoms that interact strongly with surface oxygen atoms. Increasing n_{carbons} and n_{branches} each by one (*i.e.*, increasing chain length and α-C substitution simultaneously) increases $\mathrm{p}K_{\mathrm{ia}}$ (blue lines in Fig. 4), revealing the dominant role of substitution over chain length in dictating interfacial acidity. Simply put, interfacial acidity of the alcohol is controlled more by its van der Waals interactions with the surface than the polarizability of its alkyl chain, similar to the way aqueous acidity of the alcohol is controlled more by alcohol-water interactions than polarizability effects.

To examine the effect of increasing surface temperature on interfacial acidity, we calculated K_{ia} and $\mathrm{p}K_{\mathrm{ia}}$ at 500 K. As shown in Table S17 and Fig. S14 of the ESI,‡ K_{ia} ($\mathrm{p}K_{\mathrm{ia}}$) of each alcohol is lower (greater) at 500 K than at 298 K, primarily due to a decrease in the ratio of the electronic partition functions with temperature. The weaker acidity of the alcohols ultimately signifies the greater relative population of the hydrogen-bonded species at higher temperature, suggesting that this intermediate might play an important role in surface-promoted transformations of the alcohol at catalytically relevant temperatures. While the pK_{ia} of each studied alcohol on STO(100) increases with temperature, the variations in pK_{ia} with n_{carbons} and n_{branches} remain unchanged between 298 K and 500 K (see Fig. S14 of the ESI‡), thereby demonstrating that the relationships between the interfacial alcohol–STO geometries and the resulting K_{ia} are preserved over a wide range of temperature.

4 Conclusions

In summary, we determined the driving forces governing the interfacial Brønsted–Lowry acidity of small alkanols adsorbed on STO(100) using a combination of SFG and DFT methods. Our work shows that the structure–acidity relationships in the alkanols are overall qualitatively different at the gas–oxide interface as compared to homogeneous gas and aqueous phases. The similarities with chain-length dependence in gas-phase acidity and alkyl-substituent dependence in aqueous acidity demonstrate that interfacial acidity produces a unique combination of contrary chemical trends observed in the two homogeneous phases. Our results show the critical and oft-overlooked role played by hydrogen bonding in controlling acidity at gas–solid interfaces and indicate its importance in acid–base transformations of alcohols on oxide surfaces at higher surface temperatures. Notably, the increase in relative population of the hydrogen-bonded chemisorbed intermediate with temperature, predicted computationally for all studied alcohols, strongly suggests that this intermediate is present for various small alcohols on STO(100) at catalytically relevant surface temperatures. Therefore, the equilibrium between the hydrogen-bonded and hydrogen-bond-broken chemisorbed species revealed by our computational and experimental results could play an important role in chemical transformations of alcohols on oxide surfaces. The conceptualization of interfacial acidity is generalizable to other interfaces and protic acids, permitting a comparison of acidity of different molecules on a given surface, and, ultimately, broadening the description of a fundamentally important chemical property central to understanding chemical transformations at a range of heterogeneous environments.

Author contributions

R. C. C., K. R. M., and S. R. performed the computational component of the research. A. U. C. and B. D. designed, carried out and analyzed SFG measurements. R. L. S. prepared and characterized the STO samples.

Conflicts of interest

There are no conflicts to declare.

Acknowledgements

Computations of the adsorption steps of isopropanol on STO(100) were supported by the UT-ORNL Joint Directed Research and Development (JDRD) Program of the Tennessee Science Alliance. Computations of the adsorption steps on other alkanols on STO(100) and calculations of interfacial acidity were supported by the National Science Foundation CAREER grant CHE-1753273. Computations were performed using resources at the Center for Functional Nanomaterials, a U.S. DOE Office of Science Facility, and the Scientific Data and Computing Center, a component of the Computational Science Initiative, at Brookhaven National Laboratory under Contract No. DE-SC0012704. A. U. C. and B. D. were supported by the U.S. Department of Energy, Office of Science, Basic Energy Sciences, Chemical Sciences, Geosciences, and Biosciences Division. R. L. S. was supported by the Department of Energy, Office of Science, Basic Energy Sciences, Materials Sciences and Engineering Division. S. R. thanks John E. Bartmess for discussions on alcohol acidity in gaseous and aqueous phases.

References

1 F. Polo-Garzon and Z. Wu, *J. Mater. Chem. A*, 2018, **6**, 2877–2894.
2 S. Sugunan and V. Meera, *React. Kinet. Catal. Lett.*, 1997, **62**, 327–332.
3 G. S. Foo, Z. D. Hood and Z. Wu, *ACS Catal.*, 2018, **8**, 555–565.
4 R. Hammami, H. Batis and C. Minot, *Surf. Sci.*, 2009, **603**, 3057–3067.
5 G. S. Foo, F. Polo-Garzon, V. Fung, D.-E. Jiang, S. H. Overbury and Z. Wu, *ACS Catal.*, 2017, **7**, 4423–4434.
6 F. A. Rabuffetti, P. C. Stair and K. R. Poeppelmeier, *J. Phys. Chem. C*, 2010, **114**, 11056–11067.
7 M. Daturi, G. Busca and R. J. Willey, *Chem. Mater.*, 1995, **7**, 2115–2126.
8 J. N. Kuhn and U. S. Ozkan, *J. Catal.*, 2008, **253**, 200–211.
9 J. Kubo and W. Ueda, *Mater. Res. Bull.*, 2009, **44**, 906–912.
10 M. A. Aramendıa, V. Borau, C. Jiménez, J. M. Marinas, A. Porras and F. J. Urbano, *J. Catal.*, 1996, **161**, 829–838.
11 A. Gervasini and A. Auroux, *J. Catal.*, 1991, **131**, 190–198.
12 J. E. Rekoske and M. A. Barteau, *J. Catal.*, 1997, **165**, 57–72.
13 P. N. Trikalitis and P. J. Pomonis, *Appl. Catal., A*, 1995, **131**, 309–322.
14 T. K. Varadarajan, R. Sumathi and B. Viswanathan, *Indian J. Chem., Sect. A: Inorg., Bio-inorg., Phys., Theor. Anal. Chem.*, 2001, **40**, 1033–1036.
15 S. Tan, M. B. Gray, M. K. Kidder, Y. Cheng, L. L. Daemen, D. Lee, H. N. Lee, Y.-Z. Ma, B. Doughty and D. A. Lutterman, *ACS Catal.*, 2017, **7**, 8118–8129.
16 F. Polo-Garzon, S.-Z. Yang, V. Fung, G. S. Foo, E. E. Bickel, M. F. Chisholm, D.-E. Jiang and Z. Wu, *Angew. Chem., Int. Ed.*, 2017, **129**, 9952–9956.
17 A. Ge, P. E. Videla, B. Rudshteyn, Q. Liu, V. S. Batista and T. Lian, *J. Phys. Chem. C*, 2018, **122**, 13944–13952.

18 J. H. Jang, F. Lydiatt, R. Lindsay and S. Baldelli, *J. Phys. Chem. A*, 2013, **117**, 6288–6302.

19 A.-a. Liu, S. Liu, R. Zhang and Z. Ren, *J. Phys. Chem. C*, 2015, **119**, 23486–23494.

20 R. Zhang, J. Dong, T. Luo, F. Tang, X. Peng, C. Zhou, X. Yang, L. Xu and Z. Ren, *J. Phys. Chem. C*, 2019, **123**, 17915–17924.

21 B. Doughty, S. Goverapet Srinivasan, V. S. Bryantsev, D. Lee, H. N. Lee, Y.-Z. Ma and D. A. Lutterman, *J. Phys. Chem. C*, 2017, **121**, 14137–14146.

22 S. Schmidt, G. Greczynski, C. Goyenola, G. Gueorguiev, Z. Czigány, J. Jensen, I. Ivanov and L. Hultman, *Surf. Coat. Technol.*, 2011, **206**, 646–653.

23 D. G. Sangiovanni, G. K. Gueorguiev and A. Kakanakova-Georgieva, *Phys. Chem. Chem. Phys.*, 2018, **20**, 17751–17761.

24 J. P. Perdew, K. Burke and M. Ernzerhof, *Phys. Rev. Lett.*, 1996, **77**, 3865–3868.

25 J. P. Perdew, K. Burke and M. Ernzerhof, *Phys. Rev. Lett.*, 1996, **78**, 1396.

26 S. Grimme, J. Antony, S. Ehrlich and H. Krieg, *J. Chem. Phys.*, 2010, **132**, 154104.

27 S. Grimme, S. Ehrlich and L. Goerigk, *J. Comput. Chem.*, 2011, **32**, 1456–1465.

28 G. Kresse and J. Furthmüller, *Comput. Mater. Sci.*, 1996, **6**, 15–50.

29 G. Kresse and J. Hafner, *Phys. Rev. B: Condens. Matter Mater. Phys.*, 1993, **47**, 558–561.

30 G. Kresse and J. Hafner, *Phys. Rev. B: Condens. Matter Mater. Phys.*, 1994, **49**, 14251–14269.

31 P. E. Blöchl, *Phys. Rev. B: Condens. Matter Mater. Phys.*, 1994, **50**, 17953–17979.

32 G. Kresse and D. Joubert, *Phys. Rev. B: Condens. Matter Mater. Phys.*, 1999, **59**, 1758–1775.

33 S. L. Dudarev, G. A. Botton, S. Y. Savrasov, C. J. Humphreys and A. P. Sutton, *Phys. Rev. B: Condens. Matter Mater. Phys.*, 1998, **57**, 1505–1509.

34 K. v. Benthem, C. Elsässer and R. H. French, *J. Appl. Phys.*, 2001, **90**, 6156–6164.

35 E. N. Maslen, N. Spadaccini, T. Ito, F. Marumo and Y. Satow, *Acta Crystallogr., Sect. B: Struct. Sci.*, 1995, **51**, 939–942.

36 H. J. Monkhorst and J. D. Pack, *Phys. Rev. B: Condens. Matter Mater. Phys.*, 1976, **13**, 5188–5192.

37 P. Pulay, *Chem. Phys. Lett.*, 1980, **73**, 393–398.

38 G. Henkelman, B. P. Uberuaga and H. Jónsson, *J. Chem. Phys.*, 2000, **113**, 9901–9904.

39 A. U. Chowdhury, F. Liu, B. R. Watson, R. Ashkar, J. Katsaras, C. Patrick Collier, D. A. Lutterman, Y.-Z. Ma, T. R. Calhoun and B. Doughty, *Opt. Lett.*, 2018, **43**, 2038–2041.

40 A. U. Chowdhury, B. R. Watson, Y.-Z. Ma, R. L. Sacci, D. A. Lutterman, T. R. Calhoun and B. Doughty, *Rev. Sci. Instrum.*, 2019, **90**, 033106.

41 A. Bera, D. Bullert and E. Hasselbrink, *J. Phys. Chem. C*, 2020, **124**, 16069–16075.

42 A. Bera, D. Bullert, M. Linke and E. Hasselbrink, *J. Phys. Chem. C*, 2021, **125**, 7721–7727.

43 H.-F. Wang, L. Velarde, W. Gan and L. Fu, *Annu. Rev. Phys. Chem.*, 2015, **66**, 189–216.

44 B. Hammer, L. B. Hansen and J. K. Nørskov, *Phys. Rev. B: Condens. Matter Mater. Phys.*, 1999, **59**, 7413–7421.

45 J. I. Brauman and L. K. Blair, *J. Am. Chem. Soc.*, 1968, **90**, 6561–6562.

46 J. I. Brauman and L. K. Blair, *J. Am. Chem. Soc.*, 1970, **92**, 5986–5992.

47 J. E. Bartmess, J. A. Scott and R. T. McIver, *J. Am. Chem. Soc.*, 1979, **101**, 6046–6056.

48 G. Boand, R. Houriet and T. Gaumann, *J. Am. Chem. Soc.*, 1983, **105**, 2203–2206.

49 S. B. Ghale, J. G. Lanorio, A. A. Nickel and K. M. Ervin, *J. Phys. Chem. A*, 2018, **122**, 7797–7807.